SUPPLEMENTARY INFORMATION
doi:10.1038/nature16934

Super-catastrophic disruption of asteroids at small perihelion distances

Mikael Granvik, Alessandro Morbidelli, Robert Jedicke, Bryce Bolin, William F. Bottke, Edward Beshore, David Vokrouhlický, Marco Delbò, & Patrick Michel

Orbital steady-state distributions

We obtained initial conditions for the test asteroids from the known main-belt objects (MBO) with absolute magnitudes H smaller than the assumed completeness limit. We divided the main asteroid belt in two components, because the completeness level varies substantially between the inner and outer parts of the belt. For MBOs interior to the 3:1 mean-motion resonance (MMR) with Jupiter (centered at $a \sim 2.5\,\mathrm{au}$) we selected all non-NEOs with $H < 15.9$ from MPC's list of asteroid orbital elements (MPCORB.DAT). Exterior to the 3:1 MMR we selected all non-NEOs that have $H < 14.4$ and $a < 4.1\,\mathrm{au}$ from the same file. These criteria were iteratively adjusted to result in a set of objects that were discovered prior to Jan 1, 2012. To guarantee a reasonable accuracy for the orbital elements and H magnitudes we also required that the selected objects had been observed for at least 30 days. We note that while the H magnitudes may have errors of some tenths of magnitudes it is more important that any systematic effects affect all objects in a similar way. The search resulted in 78,355 different objects. To increase the sample of Hungaria and Phocaea asteroids we cloned them 7 and 3 times, respectively, by keeping (a, e, i) constant and adding uniform random deviates $-0.001\,\mathrm{rad} < \epsilon < 0.001\,\mathrm{rad}$ to (Ω, ω, M_0). The cloning increased the total number of test asteroids to 92,449 (Fig. S2).

We reduce the full complexity and 3D vectorial character of the Yarkovsky thermal force — a recoil force arising from the re-emission of thermal photons — to a transverse force with the principal orbital effect identical to that of the full thermal force, namely a slow drift $\overline{da/dt}$ in semimajor axis a. This is the most important long-term effect relevant for our work. The same approach has been used for the orbital reconstruction of young asteroid families[23] and pairs[24], and for accurate orbital determination of NEOs[25].

Apart from the simplicity in its formulation, this implementation of the thermal force has the advantage of reducing the number of fundamental parameters. In particular, we assumed that the secular change in semimajor axis depends solely on the asteroid's size D and obliquity γ of its spin axis, $\overline{da/dt}(D, \gamma)$. Moreover, since the diurnal variant of the Yarkovsky effect nearly always dominates, and all bodies considered in this study are much larger

than the penetration depth of the thermal waves[26], $\overline{da/dt}(D,\gamma) = (\overline{da/dt})_0\,(D_0/D)\cos\gamma$, where $(\overline{da/dt})_0$ is the canonical value of the secular drift for an asteroid of a reference size D_0. Assuming a characteristic bulk density of 2 g/cm^3, a typical surface thermal inertia $\Gamma \simeq 200$ J/m^2/s$^{1/2}$/K for kilometer size asteroids[27], a rotation period of a few to a few tens of hours, and a low-eccentricity orbit with $a \sim 2.5$ au, $(\overline{da/dt})_0 \simeq 2\times10^{-4}$ au/ Myr for $D_0 = 1$ km. Observational evidence indicates that small asteroids have a bimodal obliquity distribution[28] so we use $\overline{da/dt} \simeq \pm(\overline{da/dt})_0$.

We integrated the entire set of 92,449 test asteroids for up to 100 Myr with a 1-day timestep including the eight planets from Mercury through Neptune as perturbers using a tailored version of the SWIFT integrator[29]. For the Yarkovsky modeling we assigned all test asteroids $D = 0.1$ km and a random spin obliquity of $\pm90°$, resulting in positive and negative maximum drift in a. We used only one diameter after numerically verifying that the escape routes are the same for all diameters. The relative importance of the escape routes (fraction of asteroids escaping through each route) can depend on D. But this is reflected in the H-distribution characteristic of the NEO population coming from each route, which we will determine later. Note also that our choice cannot induce an error in the drift rate much larger than an order of magnitude because most asteroids included in our study have $10\,\mathrm{m} < D < 1\,\mathrm{km}$. We integrated the test asteroids until they were ejected from the solar system or entered the NEO region ($q \leq 1.3$ au), and recorded the orbital elements every 10 kyr. A total of 70,708 test asteroids escaped the main asteroid belt during the 100-Myr integration and entered the NEO region (Fig. S3).

These test asteroids were then integrated further with a slightly different configuration. The inclusion of the Yarkovsky drift is unnecessary in this second phase as NEO dynamics are dominated by close planetary encounters which dwarf the statistical signal from the Yarkovsky drift. The nominal integration timestep was reduced to 12 hours, because a longer timestep did not correctly resolve close solar encounters and produced a non-negligible artefact in the (a,e) steady-state distribution. To build smooth steady-state distributions we recorded the elements of all test asteroids with a time resolution of 250 yr. These latter integrations were continued until the test asteroids collided with the Sun or a planet (Mercury through Neptune), escaped the solar system, or reached a heliocentric distance in excess of 100 au. For the last possibility we assumed that the likelihood of the test asteroid re-entering the NEO space ($a < 4.2$ au) is negligible as it would have to cross the outer planet region without being ejected from the solar system or colliding with a planet.

Finally, we grouped test asteroids leaving the asteroid belt via different escape routes that would provide similar NEO steady-state orbital distributions if taken individually. In total we consider six asteroidal source regions and escape routes. Two source regions (Hungaria and Phocaea asteroid groups) are determined by the orbital elements at the beginning of the integrations and four escape routes (the ν_6 secular resonance, and the 3:1, 5:2 and 2:1 mean-motion resonances with Jupiter) are determined using the test asteroids' orbital

elements at the instant when they are entering the NEO region, that is, when their recorded perihelion distance $q = a(1-e) \leq 1.3\,\mathrm{au}$ for the first time. We also constructed a steady-state distribution for Jupiter-family comets using integrations that account for gravitational perturbations by terrestrial planets[30] (Fig. S4).

When constructing alternative steady-state distributions that are used for modeling the catastrophic disruption of NEOs at small perihelion distance, q, we make use of the fact that an NEO's q does not typically monotonically decrease with time[7]. NEOs reaching small q may subsequently evolve into orbits with large q, or even all the way back to the main asteroid belt. This implies that the average disruption distance, $\overline{q_\star}$, can be relatively small and still have an effect at, say, $q \sim 0.7\,\mathrm{au}$ by removing the contribution from test asteroids that evolve from a small q to a large q. To find the $\overline{q_\star}$ that best reproduces the observed q distribution, we fit for model parameters using alternative steady-state distributions with $\overline{q_\star}$ ranging from $0.00465\,\mathrm{au}$ to $0.2\,\mathrm{au}$ (1–43 solar radii).

Observational selection effects

There are two main challenges in estimating survey selection effects, or biases, for asteroids. First, asteroid surveys have focused more on ambitiously discovering new objects at the expense of rigorously quantifying their detection capability as a function of apparent magnitude and rate of motion. These are the two main observables that determine whether an asteroid is discovered and they depend directly on the object's orbit and absolute magnitude and are required for an accurate determination of the bias. We solved this problem by restricting ourselves to the NEOs detected by CSS, which did a careful job in keeping a log of their pointing history and quantifying the limiting magnitude on a nightly basis. Second, even when all data are available as in the case of CSS, it is computationally expensive to estimate a bias correction whose result is not dominated by inaccuracy of the numerical computation technique (e.g., small number statistics).

Here, the second issue is addressed by introducing a technique that essentially maps out the orbital-element phase space of objects that can be detected in individual survey fields. The technique is here applied to the CSS, but it can be applied to any well-characterized asteroid survey that provides the detection efficiency on a nightly basis and, preferably, as a function of a detection's trail length.

Let $\boldsymbol{z} \equiv (a, e, i, \Omega, \omega, M_0, H)$ represent the set of six orbit elements and the absolute magnitude. The total number n of (perhaps multiple) detected objects in the range $[\boldsymbol{z}_1, \boldsymbol{z}_2]$ can be written as

$$n(\boldsymbol{z}_1, \boldsymbol{z}_2)\Delta\boldsymbol{z} = B(\boldsymbol{z}_1, \boldsymbol{z}_2)N(\boldsymbol{z}_1, \boldsymbol{z}_2)\Delta\boldsymbol{z}\,, \qquad (1)$$

where B refers to the survey bias, which is a properly weighted correction factor relating the number of detected objects n to the actual number of objects N in the same range. The

bias can be evaluated with a Monte Carlo simulation but doing so would be computationally expensive. Instead the bias is numerically integrated[5]. Some reasonable assumptions about the behavior of the NEO population and the survey have to be made, specifically:

1. the H, (a, e, i) and (Ω, ω, M_0) distributions are separable,
2. the detection efficiency and distributions in H and (a, e, i) change smoothly and slowly, and
3. the unbiased (Ω, ω, M_0) distribution is uniform.

   Recent work [31] has shown that the NEO (Ω, ω, M_0) distribution are slightly non-uniform, but makes a negligible difference in this study.

Under these assumptions the bias is simply the sum of the angular-element-averaged per-field detection efficiencies,

$$B(a, e, i, H) = \sum_j \epsilon_j(\boldsymbol{z}, t)\,, \tag{2}$$

where j is the field identifier. We note that B can be larger than unity, because it accounts for the re-detections of, e.g., bright NEOs. We eliminated much of the possible angular-element phase space in the integration by calculating[32] which NEO orbits could appear in the field of view given the field location and an asteroid's (a, e, i).

The bias is calculated as a sum over telescope pointings, j, centered on the same part of sky covering a short interval between times t_j and t_{j+1}, the beginning and end of the exposure, respectively. The efficiency for detecting an object, ϵ_j, with $\boldsymbol{z}$ is calculated if it is in the field. ϵ_j is a function of the object's apparent magnitude, m, and rate of motion, $\dot{\theta}$. m and $\dot{\theta}$ depend on $\boldsymbol{z}$, t_j and t_{j+1}:

$$\epsilon_j(\boldsymbol{z}, t_j, t_{j+1}) = \begin{cases} \epsilon_j \left[m(\boldsymbol{z}, t_j, t_{j+1}), \dot{\theta}(\boldsymbol{z}, t_j, T_{j+1}) \right] & \text{if in the field } j \text{ between } t_j \text{ and } t_{j+1}, \text{ and} \\ 0 & \text{if not in the field.} \end{cases} \tag{3}$$

CSS has provided their nightly detection efficiencies in the form

$$\epsilon(m) = \frac{\epsilon_0}{1 + e^{(m - m_{\rm lim})/m_{\rm drop}}}\,, \tag{4}$$

where ϵ_0 is the detection efficiency for bright unsaturated objects, $m_{\rm lim}$ is the limiting magnitude at which the efficiency drops to 50% of its maximum, and $m_{\rm drop}$ characterizes the width over which the transition occurs from high to low efficiency. We restricted the CSS data and bias calculation to nights with reasonable values of ϵ_0, $m_{\rm lim}$, and $m_{\rm drop}$, and to NEOs that did not suffer from excessive trailing losses (Fig. S5).

Debiased orbit and absolute-magnitude distributions

In general, the incremental H distribution

$$N(H) = N_0 10^{\int_{H_0}^{H} \alpha(H')\, dH'}\,, \tag{5}$$

where H_0 is a reference (fixed) value, here $H_0 = 17$, N_0 (to be fitted) is the number density at the reference H_0 and $\alpha(H)$ may be a general function that accounts for variability of the power index. Assuming $\alpha(H) = \alpha_0 =$ constant would be the simplest choice of a simple power-law distribution, but the nature of the real data over the interval from $H = 17$ to $H = 25$ requires a more complex model. We opted for a quadratic approximation of

$$\alpha(H) = c_2 H^2 + c_1 H + c_0 \tag{6}$$

that may be more conveniently reorganized as

$$\alpha(H) = \alpha_{\rm min} + c(H - H_{\rm min})^2\,, \tag{7}$$

where $\alpha_{\rm min}$ is the minimum slope of the absolute magnitude distribution, c the curvature of the absolute-magnitude-slope relation, and $H_{\rm min}$ is the absolute magnitude corresponding to the minimum slope.

The long-term evolution of NEOs is dominated by close planetary encounters that dwarf the relatively weak effect from non-gravitational forces such as the Yarkovsky force. We therefore assume that there is no correlation between H and orbit for objects pertaining to source s, and split the true population $N_s(a, e, i, H)$ into a product of two components: $N_s(H)$, describing the H distribution, and $R_s(a, e, i)$, describing the normalized steady-state orbit distribution (see Sect.). Equation (1) can now be rewritten as

$$n(a, e, i, H) = B(a, e, i, H) \sum_{s=1}^{N_S} N_s(H, H_0; \boldsymbol{p}_s)\, R_s(a, e, i)\,, \tag{8}$$

where the incremental H distribution is defined as

$$N_s(H, H_0; \boldsymbol{p}_s) = N_s(H, H_0; N_{0,s}, \alpha_{\rm min,s}, H_{\rm min,s}, c_s) = N_{0,s}\, 10^{\int_{H_0}^{H} [\alpha_{\rm min,s} + c_s (H' - H_{\rm min,s})^2]\, dH'}\,. \tag{9}$$

With the orbital distributions $R_s(a, e, i)$ pre-determined, the free parameters $\boldsymbol{p}_s$ to be fitted describe the absolute-magnitude distributions for each source s. The total number of free parameters $N_{\rm free}$ is thus nominally $4N_S$.

We employ an extended maximum-likelihood (EML) scheme[33] and the simplex optimization algorithm[34] when solving Eq. (8) for the parameters $\boldsymbol{P} = (\boldsymbol{p}_1, \boldsymbol{p}_2, \ldots, \boldsymbol{p}_{N_S})$ that describe the model. Let $(n_1, n_2, \ldots, n_{N_{\rm bin}})$ be the non-zero bins in the binned version of

$n(a, e, i, H)$, and $(\nu_1, \nu_2, \ldots, \nu_{N_{\rm bin}})$ be the corresponding bins containing the expectation values, that is, the model prediction for the number of observations in each bin. The joint probability-density function (PDF) for the distribution of observations $(n_1, n_2, \ldots, n_{N_{\rm bin}})$ is given by the multinomial distribution:

$$p_{\rm joint} = n_{\rm tot}! \prod_{k=1}^{N_{\rm bin}} \frac{1}{n_k!} \left(\frac{\nu_k}{n_{\rm tot}}\right)^{n_k}, \tag{10}$$

where $\nu_k/n_{\rm tot}$ gives the probability to be in bin k. In EML the measurement is defined to consist of first obtaining

$$n_{\rm tot} = \sum_{k=1}^{N_{\rm bin}} n_k \tag{11}$$

observations from a Poisson distribution with mean $\nu_{\rm tot}$ and then distributing those observations in the histogram $(n_1, n_2, \ldots, n_{N_{\rm bin}})$. That is, the total number of detections is regarded as an additional constraint. The extended likelihood function L is defined as the joint PDF for the total number of observations $n_{\rm tot}$ and their distribution in the histogram $(n_1, n_2, \ldots, n_{N_{\rm bin}})$. The joint PDF is therefore obtained by multiplying Eq. (10) with a Poisson distribution with mean

$$\nu_{\rm tot} = \sum_{k=1}^{N_{\rm bin}} \nu_k \tag{12}$$

and accounting for the fact that the probability for being in bin k is now $\nu_k/\nu_{\rm tot}$:

$$\begin{aligned} p'_{\rm joint} &= \frac{\nu_{\rm tot}^{n_{\rm tot}} \exp(-\nu_{\rm tot})}{n_{\rm tot}!} n_{\rm tot}! \prod_{k=1}^{N_{\rm bin}} \frac{1}{n_k!} \left(\frac{\nu_k}{\nu_{\rm tot}}\right)^{n_k} \\ &= \nu_{\rm tot}^{n_{\rm tot}} \exp(-\nu_{\rm tot}) \prod_{k=1}^{N_{\rm bin}} \frac{1}{n_k!} \left(\frac{\nu_k}{\nu_{\rm tot}}\right)^{n_k} \\ &= \exp(-\nu_{\rm tot}) \prod_{k=1}^{N_{\rm bin}} \frac{\nu_k^{n_k}}{n_k!} \,. \end{aligned} \tag{13}$$

Neglecting variables that do not depend on the parameters that are solved for, the logarithm of Eq. (13), that is, the log-likelihood function, can be written as

$$\log L = -\nu_{\rm tot} + \sum_{k=1}^{N_{\rm bin}} n_k \, \log \nu_k \,, \tag{14}$$

where the first term on the right hand side emerges as a consequence of accounting for the total number of detections.

The optimum solution, in the sense of maximum log-likelihood, $\log L_{\max}$, is obtained using the simplex algorithm[34]. To ensure that an optimum solution has been found we employ two strategies. First, we use 10 or more simplexes each with a different set of initial parameters. Second, we restart each simplex optimization using the previous step's best solution until the result converges.

To estimate model uncertainties we use the best-fit model to generate at least 50 sets of synthetic NEO distributions that mimick the observed NEO distribution. We then fit the model parameters separately for each of these sets and take the RMS in the best-fit parameters as a measure for the model uncertainty.

Our NEO population model, $N(a,e,i,H) = \sum_s N_s(a,e,i,H)$, shows that there is a correlation between (a,e,i) and H. This correlation is due to differences in the H distributions from the different sources s: the number of NEOs originating in source s relative to the total number of NEOs varies with H which, in turn, implies that the source-specific (a,e,i) distribution must also change with H. We speculate that differences between the H distributions may be due to, e.g., differences in the collisional history adjacent to source regions, or different material properties leading to different outcomes in collisions and to different Yarkovsky drift rates.

In summary, the improvements compared to previous models[3,6] are that we i) constrain the models with about 30x more unique NEOs, ii) combine the data from two surveys, iii) utilize a new method for estimating the observational selection effects[5], iv) use $R_s(a,e,i)$ that are less noisy and more realistic, v) fit for source-specific H distributions $N_s(H)$, vi) extend the model to $H = 25$ which requires that we use a flexible functional form for $N_s(H)$ allowing for both constant and varying slopes, and vii) calibrate the models in an absolute sense, that is, we do not anchor the model to external constraints such as the number of large NEOs.

References

23. Nesvorný, D. & Vokrouhlický, D. New candidates for recent asteroid breakups. *Astron. J.* **132**, 1950–1958 (2006).

24. Vokrouhlický, D. & Nesvorný, D. Pairs of asteroids probably of common origin. *Astron. J.* **136**, 280–290 (2008).

25. Farnocchia, D. *et al.* Near Earth asteroids with measurable Yarkovsky effect. *Icarus* **224**, 1–13 (2013).

26. Bottke, W., Vokrouhlický, D., Rubincam, D. & Nesvorný, D. The Yarkovsky and YORP effects: Implications for asteroid dynamics. *Ann. Rev. Earth Planet. Sci.* **34**, 157–191

(2006).

27. Delbò, M., Dell'Oro, A., Harris, A., Mottola, S. & Mueller, M. Thermal inertia of near-Earth asteroids and implications for the magnitude of the Yarkovsky effect. *Icarus* **90**, 236–249 (2007).

28. Hanuš, J. *et al.* A study of asteroid pole-latitude distribution based on an extended set of shape models derived by the lightcurve inversion method. *Astron. Astrophys.* **530**, A134 (2011).

29. Levison, H. F. & Duncan, M. J. The long-term dynamical behavior of short-period comets. *Icarus* **108**, 18–36 (1994).

30. Levison, H. F., Terrell, D., Wiegert, P. A., Dones, L. & Duncan, M. J. On the origin of the unusual orbit of comet 2P/Encke. *Icarus* **182**, 161–168 (2006).

31. JeongAhn, Y. & Malhotra, R. On the non-uniform distribution of the angular elements of near-Earth objects. *Icarus* **229**, 236–246 (2014).

32. Granvik, M., Vaubaillon, J. & Jedicke, R. The population of natural Earth satellites. *Icarus* **218**, 262–277 (2012).

33. Cowan, G. *Statistical Data Analysis* (Oxford University Press, New York, U.S., 1998).

34. Nelder, J. A. & Mead, R. A simplex method for function minimization. *Computer Journal* **7**, 308–313 (1965).

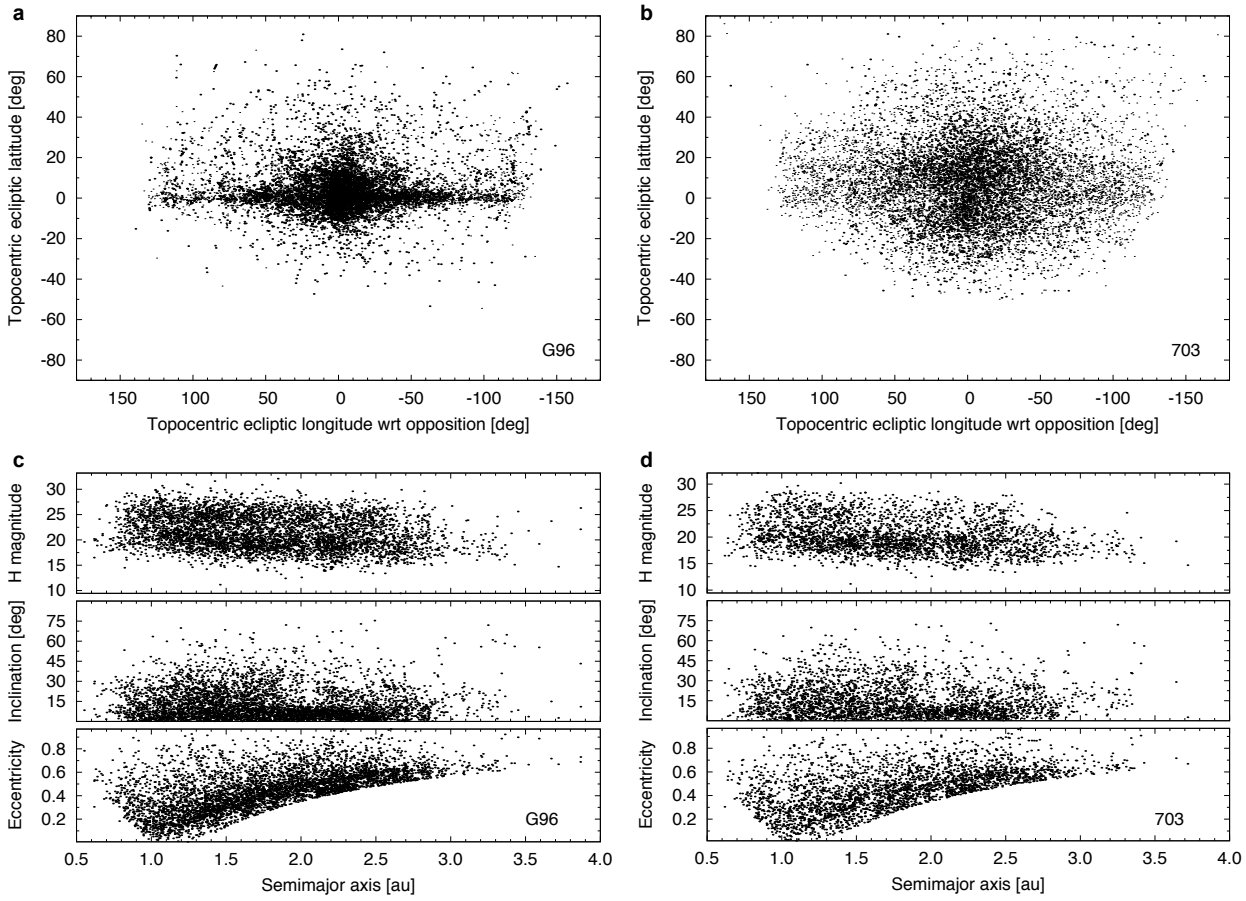

Figure S1: NEO observations with CSS during 2005–2012. Observed topocentric ecliptic cooordinates of NEOs detected by CSS's (**a**) G96 and (**b**) 703 stations. Absolute magnitude H, inclination i and eccentricity e as a function of semimajor axis a for NEOs detected on nights with good estimates for the detection efficiency by CSS's (**c**) G96 and (**d**) 703 stations. The visible dip in the observed H distribution at $H \sim 22.5$ with G96 suggests that the H distribution cannot be modeled with a power-law using a constant slope. The a, e distribution shows a clear positive bias for objects with perihelion distance $q \sim 1\,\mathrm{au}$, because they are easy to detect during close encounters with the Earth. The models are calibrated with up to 7,775 NEOs fulfilling $0.6\,\mathrm{au} < a < 3.5\,\mathrm{au}$, $0 < e < 1$, $0 < i < 76^\circ$, and $17 < H < 25$.

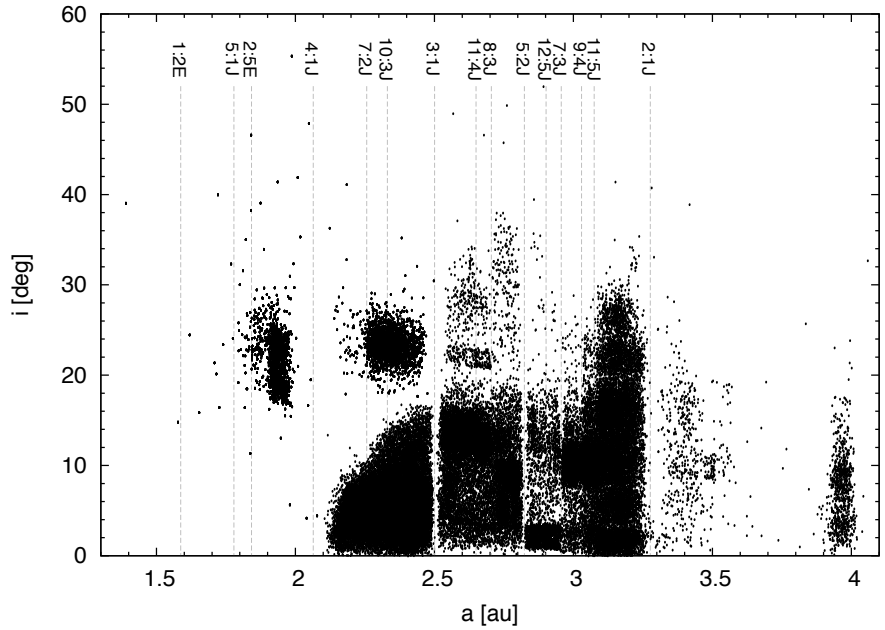

Figure S2: Initial orbit distribution for the test asteroids used in the integrations. The orbit distribution corresponds to an unbiased orbit distribution of known MBOs with a different selection criteria for orbits interior and outside the 3:1 mean-motion resonance. The verical dashed lines mark approximate locations of selected mean-motion resonances with the Earth and Jupiter.

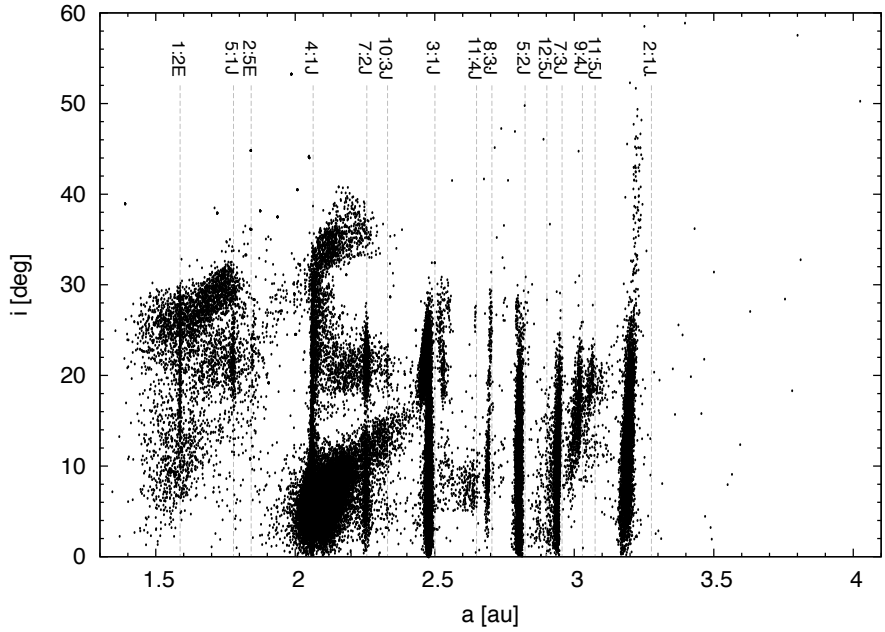

Figure S3: Orbit distribution for test asteroids that are in the process of entering the NEO region. The verical dashed lines mark approximate locations of selected mean-motion resonances with the Earth and Jupiter.

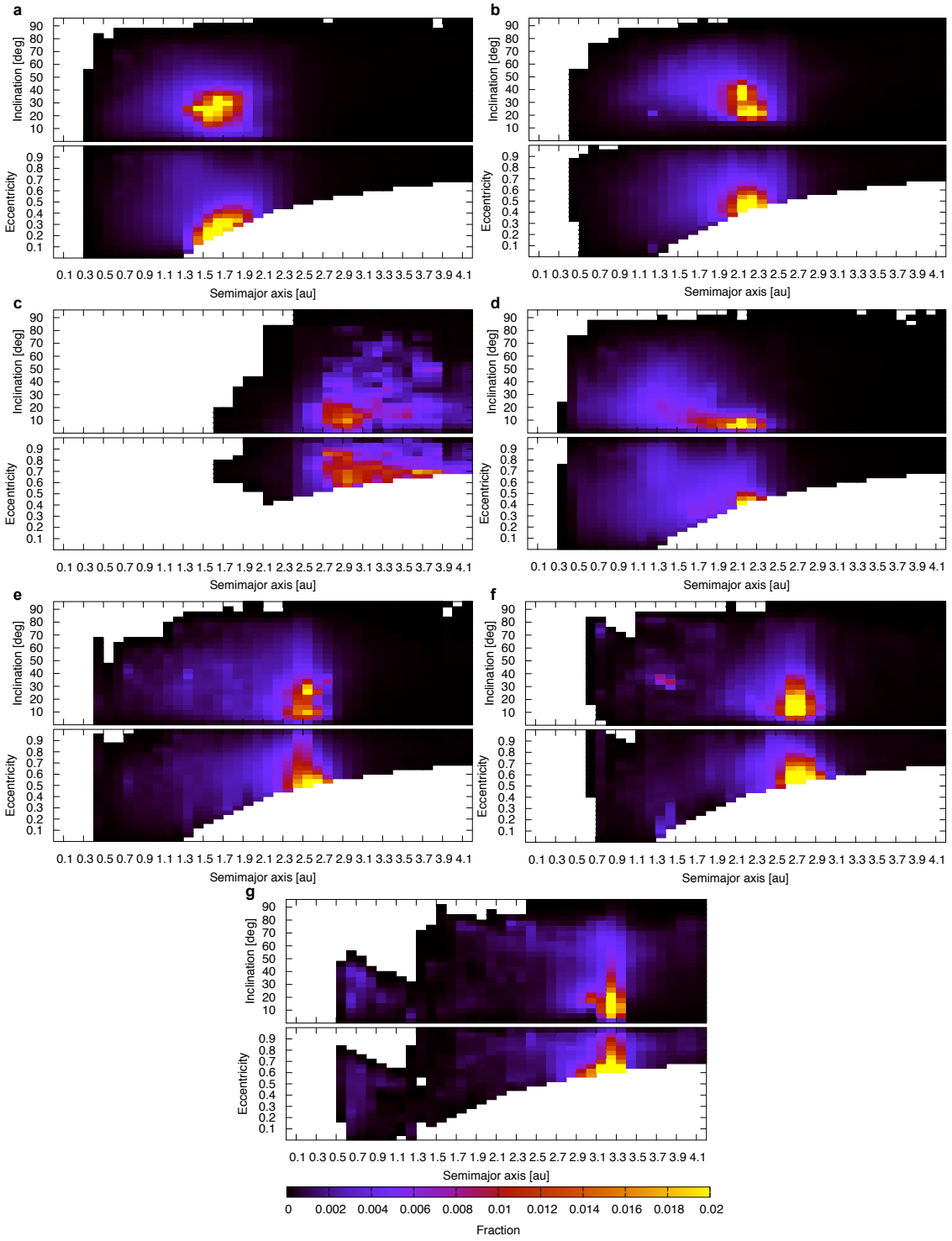

Figure S4: Orbital steady-state distributions for NEOs originating in the (a) Hungaria, (b) Phocaea and (c) JFC regions, or escaping through the (d) ν_6 secular-resonance complex (including 4:1 and 7:2 MMRs), (e) 3:1 MMR, (f) 5:2 MMR complex (including 7:3 and 8:3 MMRs), and (g) 2:1 MMR complex (including 9:4 and 11:5 MMRs, and the z_2 secular resonance).

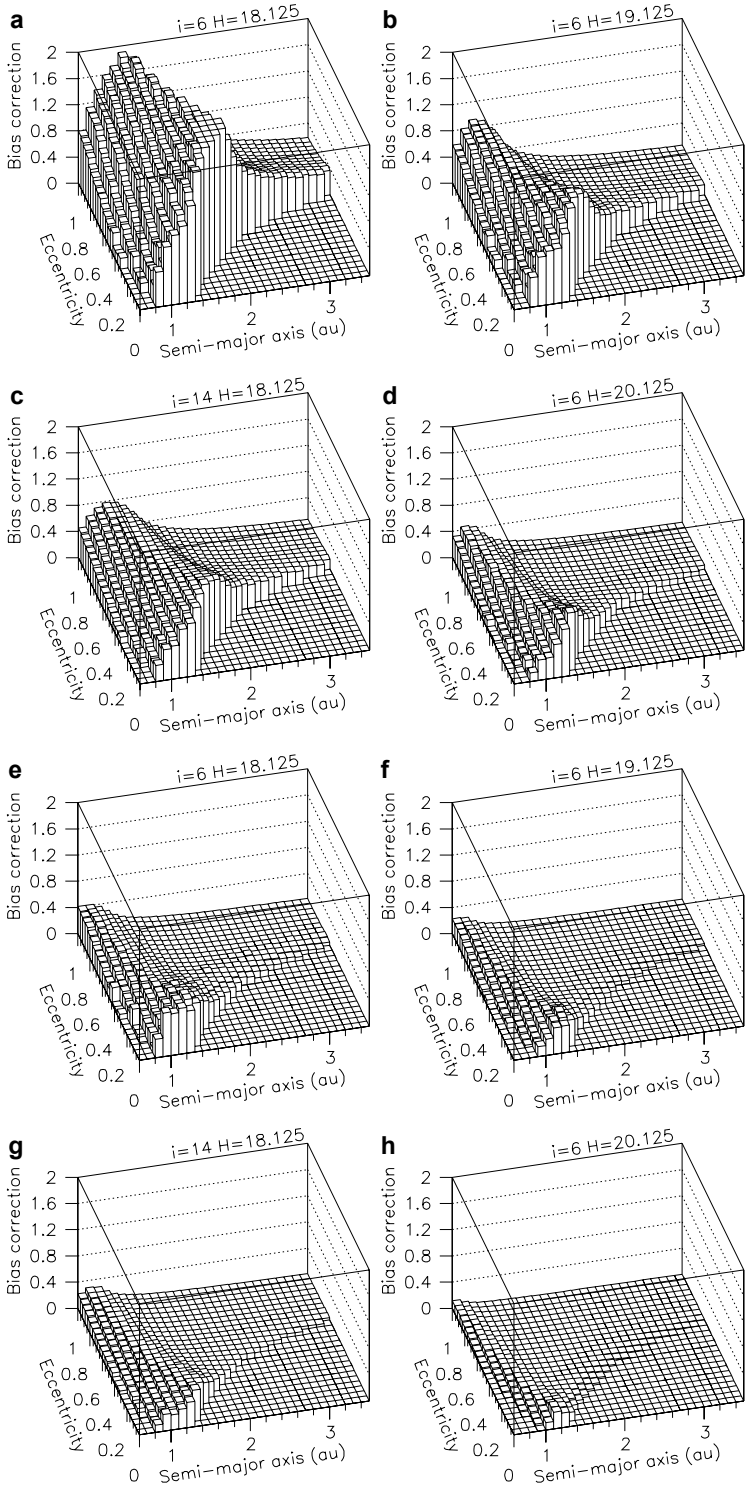

Figure S5: CSS survey bias functions. Survey bias correction as a function of semimajor axis and eccentricity for four different (i, H) combinations: $i = 6°$ and $H = 18.125$ (**a** G96, **e** 703), $i = 6°$ and $H = 19.125$ (**b** G96, **f** 703), $i = 14°$ and $H = 18.125$ (**c** G96, **g** 703), and $i = 6°$ and $H = 20.125$ (**d** G96, **h** 703).

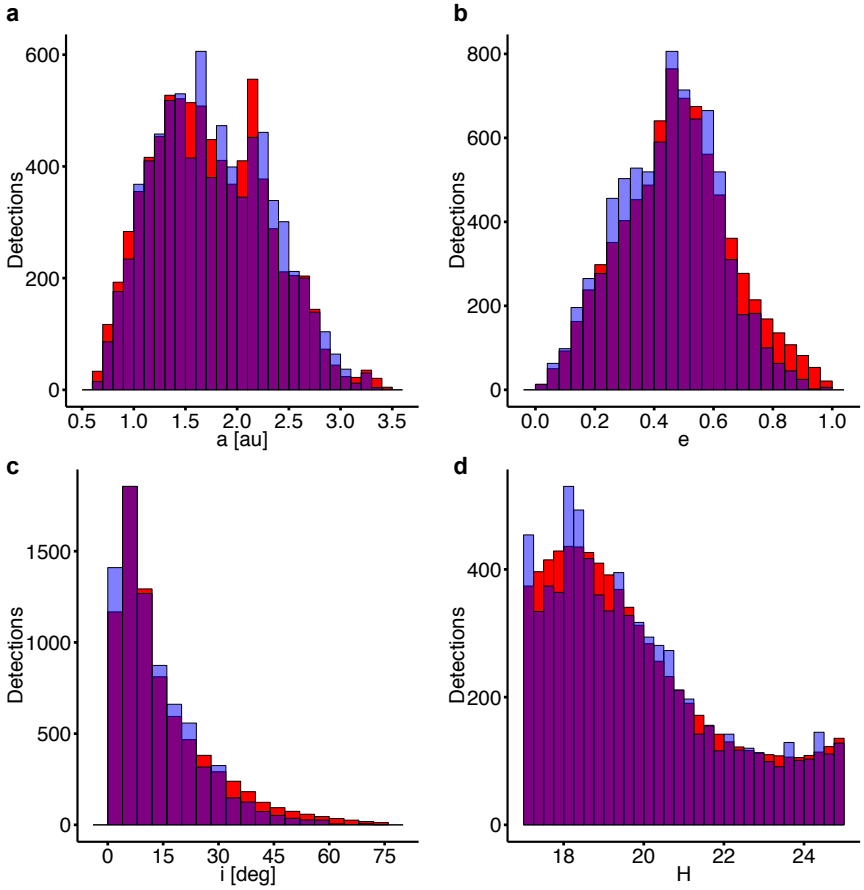

Figure S6: Observed and predicted NEO parameter distributions. The observed (blue) and biased 7-source-model predictions (red) for NEO (**a**) semimajor axis, (**b**) eccentricity, (**c**) inclination, and (**d**) absolute magnitude distributions when utilizing both 703 and G96 data.

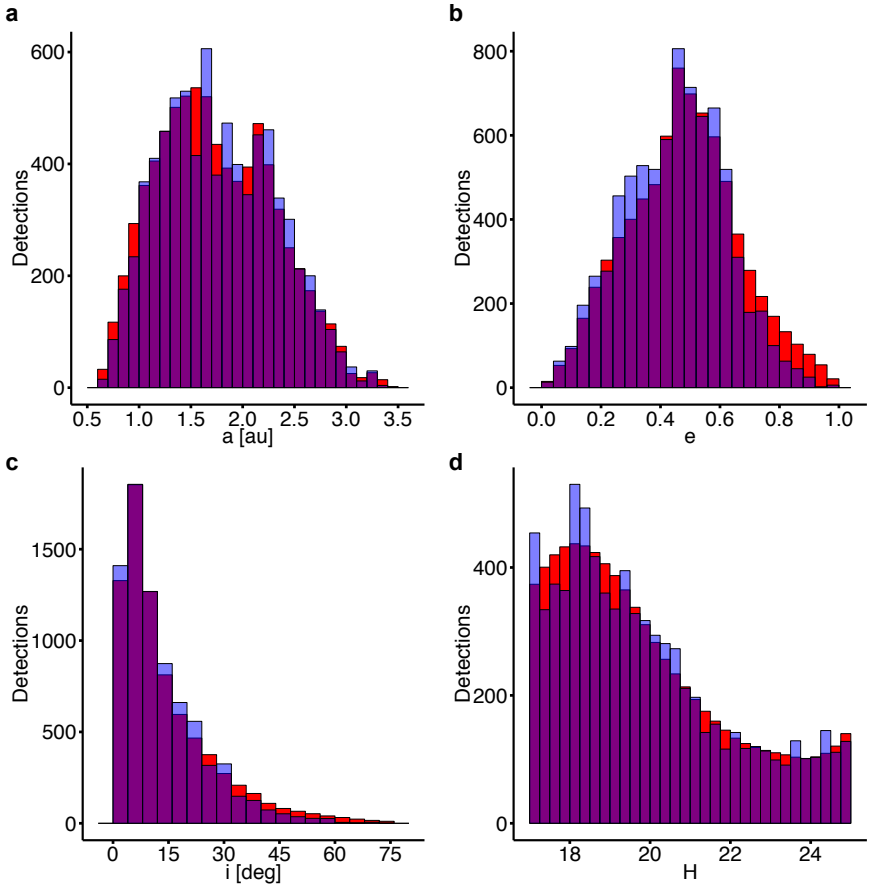

Figure S7: Observed and predicted NEO parameter distributions. The observed (blue) and biased 24-source-model predictions (red) for NEO (**a**) semimajor axis, (**b**) eccentricity, (**c**) inclination, and (**d**) absolute magnitude distributions when utilizing both 703 and G96 data.

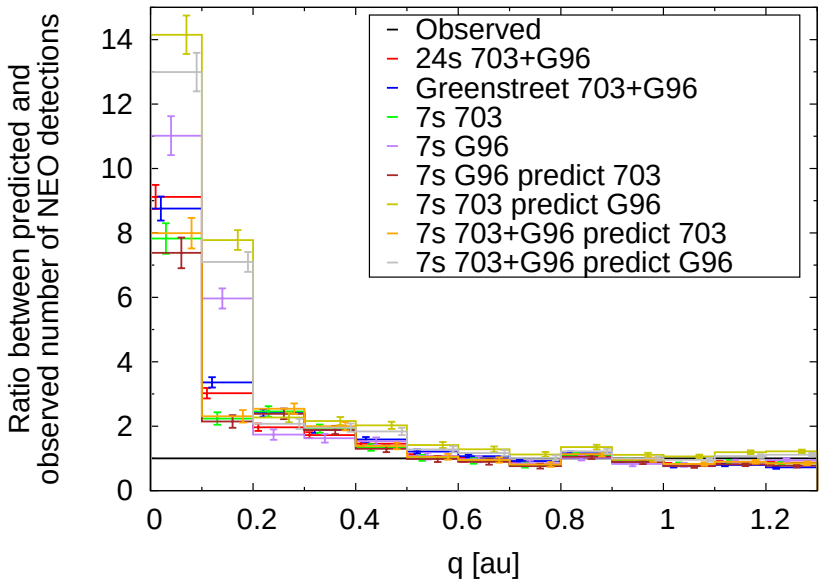

Figure S8: Observed and predicted perihelion distances for NEOs. The ratio between the observed and predicted number of NEO detections by CSS as a function of perihelion distance, q. The horizontal black line is the reference which would be obtained by a model that exactly reproduces the observed distribution. The other lines are predictions based on models that do not account for a disruption near the Sun: a biased 24-source model based on 703 and G96 observations compared with 703 and G96 observations; a biased model based on an independent orbit model[7] based on 703 and G96 compared with 703 and G96; a biased 7-source model based on 703 compared with 703; a biased 7-source model based on G96 compared with G96; a biased 7-source model calibrated in the range $0.7\,\mathrm{au} < q < 1.3\,\mathrm{au}$ and based on G96 compared with 703; a biased 7-source model calibrated in the range $0.7\,\mathrm{au} < q < 1.3\,\mathrm{au}$ and based on 703 compared with G96; a biased 7-source model calibrated in the range $0.7\,\mathrm{au} < q < 1.3\,\mathrm{au}$ and based on 703 and G96 compared with 703; and a biased 7-source model calibrated in the range $0.7\,\mathrm{au} < q < 1.3\,\mathrm{au}$ and based on 703 and G96 compared with G96. None of the models are able to reproduce the observed q distribution but systematically show an overprediction at small q. The systematic overprediction(underprediction) of G96(703) data is also visible in the other orbital elements (Extended Data Fig. S10) and highlights the importance of combining data from complementary data sources. The error bars are computed assuming Poisson statistics.

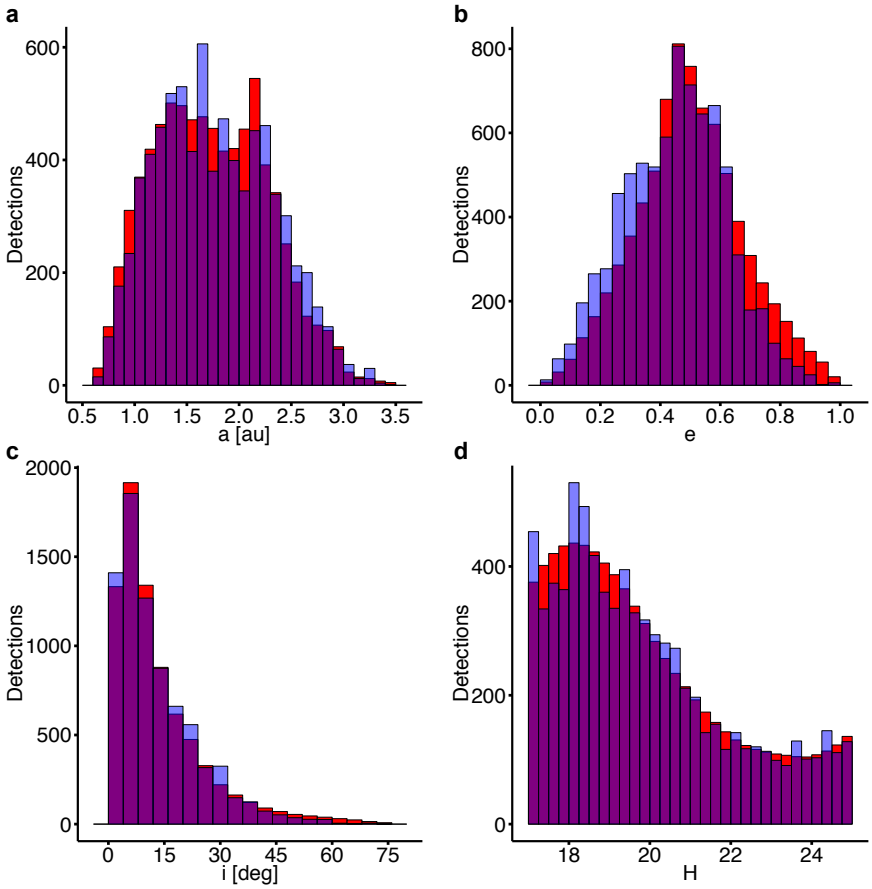

Figure S9: Observed and predicted NEO parameter distributions. The observed (blue) and biased model predictions (red) for NEO (**a**) semimajor axis, (**b**) eccentricity, (**c**) inclination, and (**d**) absolute magnitude distributions when utilizing both 703 and G96 data. The model is based on independent orbit distributions[7].

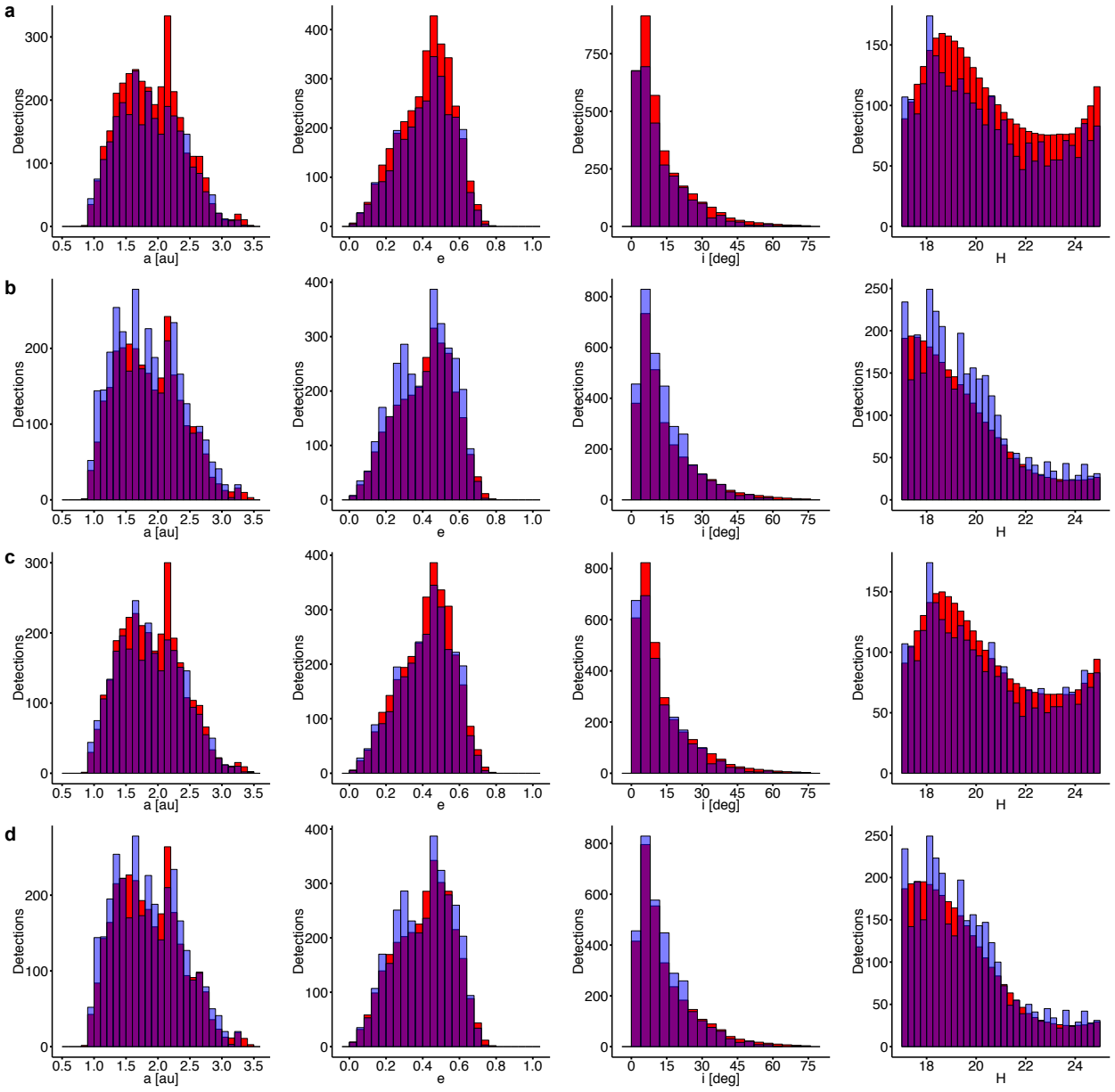

Figure S10: Observed and predicted NEO parameter distributions. Comparisons of the observed (blue) and biased model predictions (red) for NEO (a, e, i, H) distributions (columns from left to right) when using different survey combinations. **a**, The (a, e, i, H) distributions for G96 when the model is based on 703 data only. **b**, The (a, e, i, H) distributions for 703 when the model is based on G96 data only. **c**, The (a, e, i, H) distributions for G96 when the model is based on both G96 and 703 data. **d**, The (a, e, i, H) distributions for 703 when the model is based on both G96 and 703 data. The NEO model used contains 7 sources and the fit is limited to $0.7\,\mathrm{au} < q < 1.3\,\mathrm{au}$. **a** and **b** show that the adopted modeling approach is solid, and **c** and **d** that there is a clear improvement in the model accuracy when data from two complementary surveys are combined.

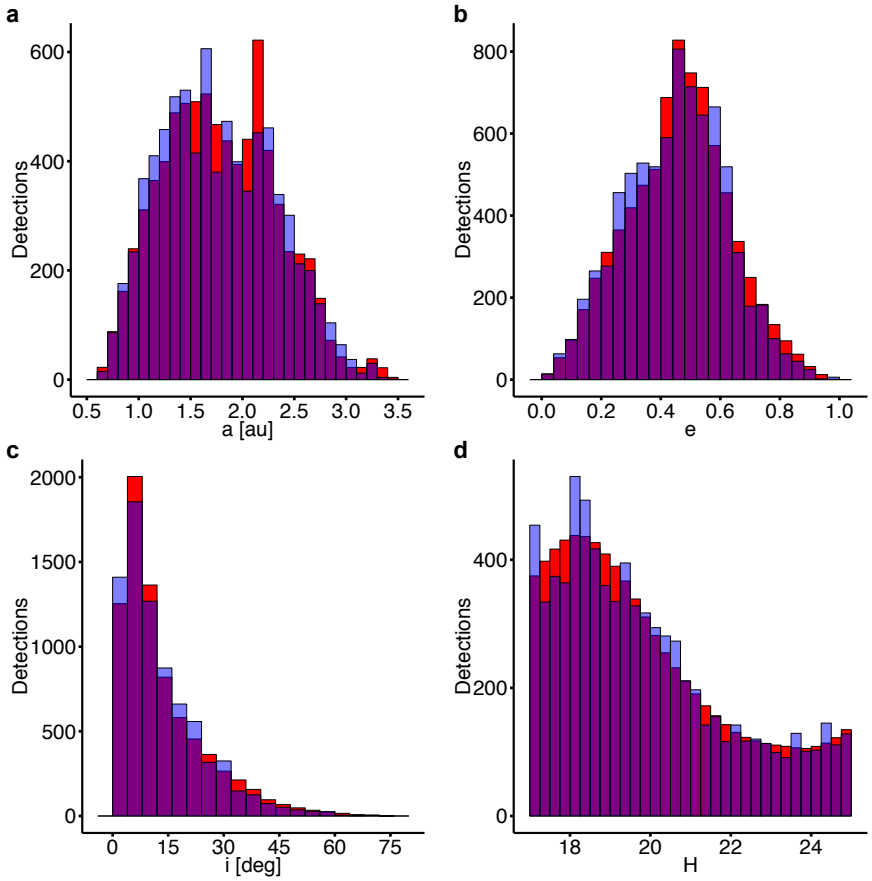

Figure S11: Observed and predicted NEO parameter distributions. The observed (blue) and biased 7-source-model predictions (red) for NEO (**a**) semimajor axis, (**b**) eccentricity, (**c**) inclination, and (**d**) absolute magnitude distributions when utilizing both 703 and G96 data and assuming $\overline{q_\star} = 0.076$ au.

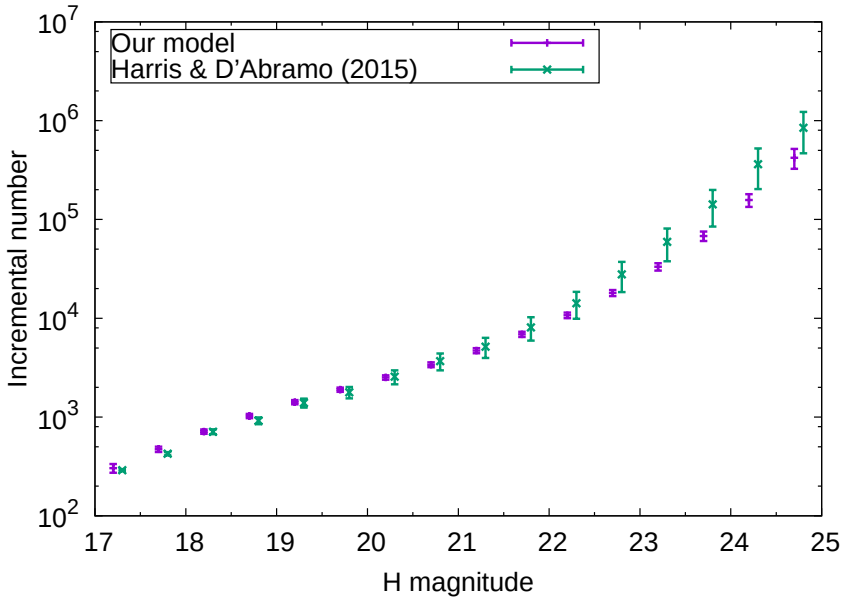

Figure S12: Debiased absolute-magnitude distributions for NEOs. The incremental debiased H distribution when assuming $\overline{q_\star} = 0.076\,\mathrm{au}$ compared to the most recent independent estimate[8] for the debiased H distribution. The symbols have been offset by ± 0.05 magnitudes from the bin centers. The error bars are ± 1 standard deviation.

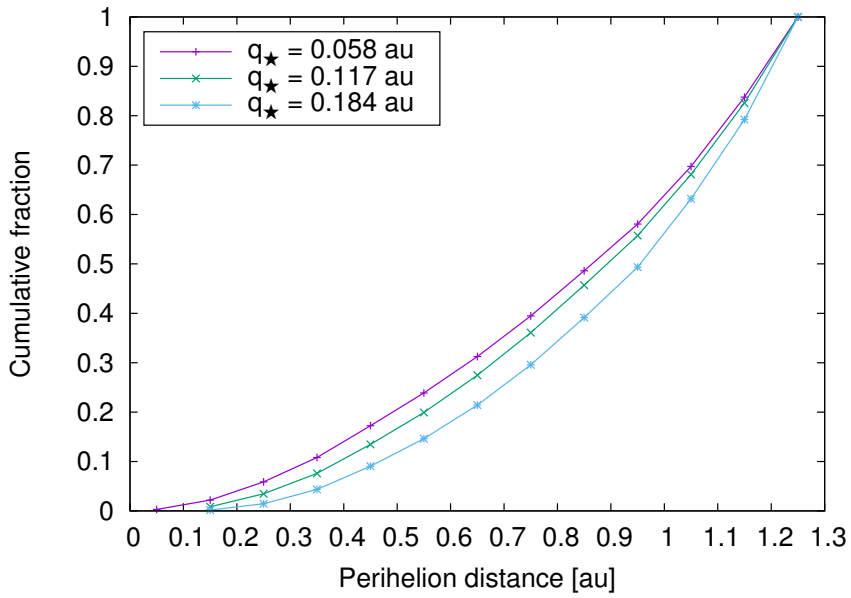

Figure S13: Debiased cumulative perihelion-distance distributions for NEOs based on the best-fit NEO population models. The different symbols refer to different assumptions for the disruption distance, $q_\star$. The lines connecting the symbols are only provided for reference. Note that an increasing disruption distance leads to a steeper slope for the perihelion-distance distribution.

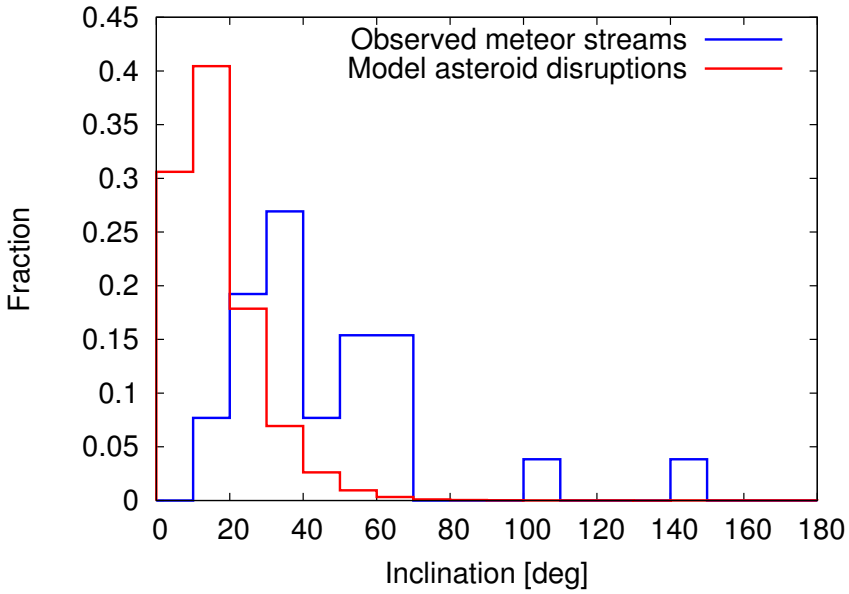

Figure S14: Inclination distributions for meteor streams and simulated disrupting asteroids. The inclination distribution for meteor streams with $q < 0.184\,\mathrm{au}$ identified in Canadian Meteor Orbit Radar (CMOR) data[17,18] (blue) and the combined inclination distribution for model asteroid disruptions when assuming $\overline{q_\star} = 0.058\,\mathrm{au}$, $\overline{q_\star} = 0.117\,\mathrm{au}$ or $\overline{q_\star} = 0.184\,\mathrm{au}$ (red). High-speed meteors are easier to detect with radar and the orbital distribution is therefore biased against low-inclination orbits. Yet most of the meteor streams identified in CMOR data have low-to-moderate inclinations typical for asteroid disruptions. Meteor streams with $i \gtrsim 90^\circ$ are most likely caused by disruptions of comets, although we cannot rule out an origin in an asteroid disruption. Only 7 of the 33 meteor streams identified in CMOR data have been linked to possible parent bodies — three to comets and four to (3200) Phaethon or its proposed[18] fragments, (155140) 2005 UD and 2004 QX_2. The majority of the unlinked meteor streams agree with an origin in an asteroid disruption and the lack of obvious parent bodies suggest that they have disrupted super-catastrophically with the largest fragment containing substantially less than 50% of the parent's mass and is thus too small to be detected with current assets.